Applied Catalysis A: General 526 (2016) 21–27

Contents lists available at ScienceDirect

Applied Catalysis A: General

journal homepage: www.elsevier.com/locate/apcata

Catalytic effect of Bi^{5+} in enhanced solar water splitting of tetragonal $BiV_{0.8}Mo_{0.2}O_4$

Rajini P. Antony[a], Tom Baikie[b], Sing Yang Chiam[c], Yi Ren[c], Rajiv Ramanujam Prabhakar[b], Sudip K. Batabyal[b], Say Chye Joachim Loo[a,**], James Barber[d,**], Lydia Helena Wong[a,c,*]

[a] School of Materials Science and Engineering, Nanyang Technology University, Singapore
[b] Energy Research Institute @ NTU (ERI@N), Nanyang Technological University, Research Techno Plaza, Singapore 637553, Singapore
[c] Institute of Materials Research and Engineering(IMRE), Agency of Science, Technology, and Research (A*Star), 3 Research Link, Singapore 117602, Singapore
[d] Division of Molecular Biosciences, Imperial College London, London, United Kingdom

ARTICLE INFO

Article history:
Received 5 May 2016
Received in revised form 20 July 2016
Accepted 22 July 2016
Available online 22 July 2016

Keyword:
Photoelectrochemical water splitting
Solar water oxidation
Bismuth vanadate
Phase transition
Tetragonal scheelite

ABSTRACT

Improved photoelectrochemical activity for tetragonal $BiV_{0.8}Mo_{0.2}O_4$ fabricated by hydrothermal synthesis is reported in the present study. The enhanced water oxidation efficiency is attributed to the formation of cation vacancies (Bi^{5+})/oxygen interstitials due to high amount of Mo doping. Efficient charge transport and electron hole separation for water oxidation using $BiV_{0.8}Mo_{0.2}O_4$ photoanode was supported by electrochemical impedance investigations and open circuit photovoltage measurements. The present study gives a significant insight into the role of nonstoichiometry related efficient water oxidation using tetragonal $BiVO_4$.

1. Introduction

Direct conversion of solar to chemical energy can be achieved by using Photoelectrochemical (PEC) cells and is important for the challenge to generate renewable fuels. For this technology to come to fruition it is necessary to develop efficient inorganic semiconductors [1], [2], [3], [4] and [5] which satisfies the requirement for efficient water splitting. $BiVO_4$ is one such material, which has a suitable band gap in the visible range and shows resistance against photo corrosion [6]. Among different crystal structures, the monoclinic scheelite phase is reported to possess superior photocatalytic activity [6] and [7] and has better hole conductivity [8]. The conduction band of $BiVO_4$ is near 0.0 V vs Reversible Hydrogen Electrode (RHE), making it suitable for water oxidation. Moreover the theoretical photocurrent that can be generated is excellent being 7.5 mA/cm^2, assuming complete absorption of photons of energies higher than 2.4 eV [9]. But the photons to current conversion efficiencies were found to be low due to its poor charge transport properties [10] and [11]. Among different methods existing [9], [12], [13], [14], [15], [16], [17] and [18], metallic doping [12], [19] and [20] was found to be an efficient way of minimizing the above mentioned problems. Mo/W doping was reported to enhance the electrical conductivity and PEC performance of $BiVO_4$, with theoretical calculations showing that Mo^{6+} and W^{6+} substitutional doping at the V^{5+} site enhances its *n*-type conductivity[9], [10], [11] [21] and [22]. Also, as the dopant concentration increases, a structural distortion for the monoclinic crystal structure eventually leads to a phase transformation to the tetragonal scheelite polymorph [23], [24], [25], [26] and [27]. It was proposed and theoretically shown that the lattice distortion of monoclinic scheelite structure creates an internal electric field which is responsible for the enhance charge separation [8]. But reports on efficient PEC performance of tetragonal $BiVO_4$ are currently limited, and its performance was normally investigated by varying the doping concentration from 0 to 8 wt% of Mo/W [9], [23], [24] and [25]. However, a decrease in the PEC performance was observed beyond 6% Mo of doping and was attributed to the appearance of tetragonal phase in $BiVO_4$.

In this paper we have studied the effect of Mo doping (ranging from 0 to 20 mol%) on the crystal structure of hydrothermally

* Corresponding author at: School of Materials Science and Engineering, Nanyang Technology University, Singapore, Division of Molecular Biosciences, Imperial College London, United Kingdom.
** Corresponding authors.
E-mail addresses: JoachimLoo@ntu.edu.sg (S.C.J. Loo), j.barber@imperial.ac.uk (J. Barber), LydiaWong@ntu.edu.sg (L.H. Wong).

http://dx.doi.org/10.1016/j.apcata.2016.07.022
0926-860X/

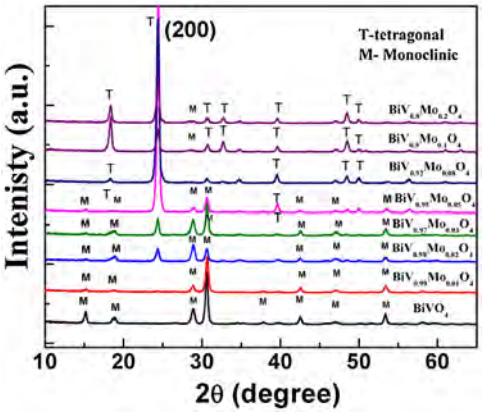

Fig. 1. X-ray diffraction pattern for pristine and Mo doped $BiVO_4$ samples showing change in crystal structure with increase in doping concentration (mol% of Mo = 0–20).

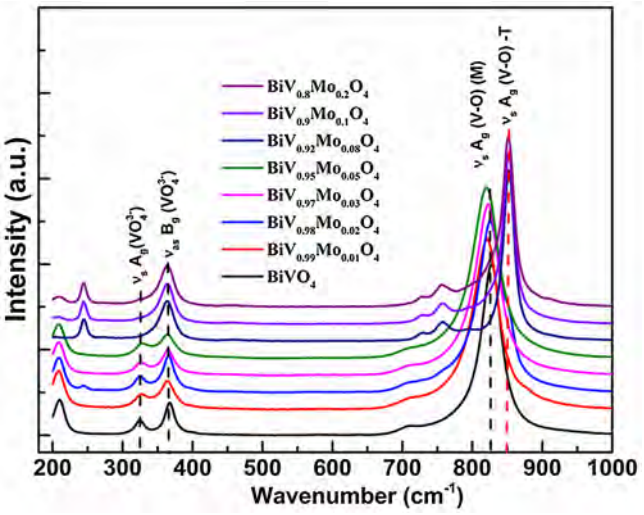

Fig. 2. Micro Raman spectra of pristine and Mo doped $BiVO_4$ photoanodes.

grown $BiVO_4$ photoanodes and the related effect on PEC performance. An enhancement in the PEC performance for the tetragonal $BiV_{0.8}Mo_{0.2}O_4$ photoanode formed by high levels of Mo doping (20 mol%) were observed for the first time and the physical processes involved were elucidated by Mott Schottky analysis, electrochemical impedance spectroscopy, open circuit photovoltage measurements and X-ray photoelectron spectroscopic analysis. The study gives insights into the doping induced phase transformation of hydrothermally grown $BiVO_4$ photoanodes and the associated PEC performance.

2. Results and discussions

$BiV_{1-x}Mo_xO_4$ photoanodes were fabricated by a hydrothermal route in which the value of 'x' was varied in the range 0–0.2. The schematic of the photoanode preparation procedure by hydrothermal route is shown in Fig. S1. The crystallinity of the pristine and doped $BiVO_4$ were verified by XRD and from the reflection positions in the XRD patterns (Fig. 1), it is evident that the pristine $BiVO_4$ possessed a monoclinic scheelite crystal structure [26]. Using a Pawley fitting method the lattice parameters of the monoclinic $BiVO_4$ were extracted as $a = 5.201(7)$ Å, $b = 5.091(3)$ Å, $c = 11.690(2)$ Å, $\gamma = 89.6(2)^\circ$ (space group $I112/b$). As the Mo doping concentration increased, the crystal structure changed from monoclinic to tetragonal, indicating tetragonal phase stabilization. This was most clearly observed by monitoring the evolution of the tetragonal (200) reflection positioned at approximately 24.5° 2θ, as indicated in Fig. 1. Also, as the intensity of the reflections of the tetragonal polymorph increased with increasing values of x, there was a corresponding reduction in intensity of the reflections associated with the monoclinic polymorph. Using the Pawley fitting technique the lattice parameters of the tetragonal polymorph were estimated as $a = 7.290(6)$ Å, $c = 6.478(7)$ Å (space group $I4_1/amdz$). The monoclinic scheelite to tetragonal scheelite phase transition can be attributed to the substitution of the larger hexavalent Mo (ionic radius = 0.41 Å) in place of pentavalent V (IR = 0.36 Å). However, from charge balancing considerations this must be accompanied with the formation of oxygen interstitials and/or cation vacancies, or the insertion of protons (see XPS section). Indeed, the isostructural material $CeNbO_{4+\delta}$ has been shown to readily accept interstitial oxygen into the crystal lattice, which is accompanied by a partial oxidation of the Ce^{3+} to Ce^{4+} [28]. The variation in valence state of the respective elements, particularly those of the bismuth and oxygen sites is discussed in further detail in the X-ray photoelectron section described later. Similar results were revealed by Zhou et al. where the solid solution dissolution of Bi^{3+} vacancies were observed up to doping concentration of x = 0.24 [26]. In the present study, we did not observe any reflections in XRD patterns, which indicated no formation of bismuth molybdate up to x = 0.20 of Mo doping. The High Resolution Transmission Electron Microscopic (HRTEM) studies conducted on $BiV_{0.8}Mo_{0.2}O_4$ revealed that it formed tetragonal crystal structure with (200) plane having a d spacing of 0.352 nm, as shown in Fig. S2. This result is consistent with the XRD pattern of $BiV_{0.8}Mo_{0.2}O_4$.

The influence of Mo doping in the crystal structure was also reflected in the micro Raman spectra. The intense peak in the micro Raman spectra (Fig. 2) positioned at ~827 cm^{-1} is assigned to the symmetric stretching vibrational mode (A_g) of V-O bond [29]. A weak shoulder at ~711 cm^{-1} corresponds to the asymmetric stretching vibrational mode of V-O bond. As the fraction of the Mo increased, the band at ~827 cm^{-1} shifted to 850 cm^{-1}, which can be ascribed to the symmetric stretching mode (A_g) of V-O bond of tetragonal $BiVO_4$ as evident from the micro Raman spectra of $BiV_{0.92}O_4Mo_{0.08}$. Similarly, a small peak at ~755 cm^{-1} became evident during the phase transformation from monoclinic to tetragonal and assigned to the asymmetric stretching mode of V-O vibration (B_g symmetry) in the tetragonal crystal structure. The peak positioned at 208 cm^{-1} corresponds to the external modes (rotation and translation) of $BiVO_4$. The peaks at ~324 and ~364.7 cm^{-1} originated from the symmetric A_g bending and asymmetric B_g bending modes of vanadate anions merged to a single peak at ~362.7 cm^{-1} as the doping concentration increased indicating phase transition from monoclinic to tetragonal. In addition, the peak at ~245 cm^{-1} in samples having higher Mo content corresponds to the stretching mode of Bi-O bond in tetragonal $BiVO_4$ and the results are in agreement with the phase transition related micro Raman investigation of $BiVO_4$ previously reported in the literature [25] and [26].

It is widely reported and accepted that the monoclinic phase of $BiVO_4$ absorbs in the visible region (band gap = 2.4 eV) and the tetragonal phase absorbs (band gap 2.7 eV) at the border between visible and UV region [6] and [29]. Light absorption observed in the monoclinic scheelite structure is in the longer wavelength region compared to that of the tetragonal system [8]. It was evident from the absorption spectra (Fig. S3), that there is a decrease in the visible light absorption as the doping concentration increased, and UV light absorption dominated in the heavily doped samples. The band gaps of different samples were calculated from the Tauc plot and were found to vary from 2.3 eV to 2.7 eV with increasing Mo concentrations indicating progressive phase transition from monoclinic

scheelite to tetragonal scheelite. The values corresponding to each doped samples are listed in Table S1 of supporting information.

FESEM micrographs of the pristine and doped $BiVO_4$ shown in Fig. 3a–h revealed that as the doping concentration increased, the microstructure of the samples gradually changed from the dodecahedral prism-like to rod-like structure. The pristine $BiVO_4$ showed a typical prism-like polyhedral shape for the monoclinic crystal structure (Fig. 3a) [7], [31] and [32]. As the doping concentration increased, there appeared rod-like structures along with the prism-like structures. When the doping concentration reached x = 0.2, complete wheat grain-like structures were formed and were arranged in a compact way (Fig. 3h). It was assumed that the morphological change was due to the phase transition induced by heavy Mo doping. A similar case was observed for the tetragonal $BiVO_4$ particles formed by 10 atom% yttrium doping reported by Usai et al. [25]. The higher surface area value (5.69 m^2/g, Table S1) for the $BiV_{0.8}Mo_{0.2}O_4$ was attributed to the formation of the rod-like structure due to the phase transition. The BET surface area values obtained for the pristine and Mo doped $BiVO_4$ samples were considerably lower, and was in accordance with the reported values (Table S1) [24] and [26]. It was also noted that the surface area for $BiV_{0.8}Mo_{0.2}O_4$ was almost twice to that of the pristine which can play a favorable role in the water oxidation performance.

Further the photoelectrochemical water oxidation activity of the Mo:$BiVO_4$ photoanodes was investigated. The amount of Mo doping was limited up to 20 atomic% for PEC investigation in the present study to rule out the effect of Bismuth molybdate formed at a concentration beyond 20% [26]. The variation of photocurrent densities of the different Mo doped $BiVO_4$ photoanodes at 1.23 V vs RHE in 0.5 M sodium sulfate (pH = 6.9) is shown in Fig. 4a. It is evident that the photocurrent densities initially increased up to a doping concentration of x = 0.03 and then start decreasing until x = 0.05. This observation was in accordance with previously reported results [33]. When the amount of Mo is above x = 0.1–0.2, the photocurrent slowly started to increase and reached maximum at a dopant concentration of x = 0.2. Fig. 4b shows the linear sweep voltamogram for the pristine and $BiV_{0.8}O_4Mo_{0.2}$ under dark and illuminated conditions. Under illuminated conditions, the photocurrent densities were 0.02 and 0.12 mA/cm^2 for the pristine and $BiV_{0.8}O_4Mo_{0.2}$ photoanodes respectively, indicating a higher PEC performance for the tetragonal $BiV_{0.8}O_4MoO_4$ photoanode. When sodium sulfite was added as an oxygen scavenger in the electrolyte, the photocurrent was enhanced to 0.89 mA/cm^2 for $BiV_{0.8}Mo_{0.2}O_4$ photoanode, which was five times higher than that of pristine photoanode (Fig. 4c). In addition, we observed a reduction in the water oxidation onset potential by 300 mV. Good photocurrent stabilities were observed for the pristine and doped samples (Fig. 5a and b), which was verified by current vs time plot under illumination conditions at a potential of 1.23 V vs RHE in Na_2SO_4 in presence and absence of hole scavenger (0.5 M Na_2SO_3). The amount of oxygen evolved during stability test corroborated with the improved water oxidation capability of $BiV_{0.8}Mo_{0.2}O_4$ compared to $BiVO_4$. IPCE spectra of pristine and $BiV_{0.8}O_4Mo_{0.2}$ photoanodes at 1.23 V versus RHE in 0.5 M Na_2SO_4 electrolyte (Fig. S5a) was also consistent with the PEC results. In comparison to pristine $BiVO_4$, $BiV_{0.8}Mo_{0.2}O_4$ exhibited higher photo activity over the entire UV−vis region. The IPCE dropped to zero at 530 nm revealing the band gaps of pristine and doped $BiVO_4$ close to 2.4 eV and the results agreed with UV Visible absorption spectra and the corresponding band gap values (Fig. S3 and Table S1). Absorbed photon to current conversion (APCE) efficiencies were calculated and showed higher efficiency for $BiV_{0.8}Mo_{0.2}O_4$, demonstrating better collection and charge separation ability as shown in Fig. S5b. The improvement in the bulk charge transport as well as the catalytic efficiency at the interface is further proved by the improved separation efficiency (Fig. S6a) and catalytic efficiency (Fig. S6b) obtained for $BiV_{0.8}Mo_{0.2}O_4$.

To understand the influence of the elemental composition on PEC performance, XPS investigations were carried out on the $BiVO_4$, $BiV_{0.95}Mo_{0.05}O_4$ and $BiV_{0.8}Mo_{0.2}O_4$ photoanodes and the high resolution XPS spectra of Bi, V, O and Mo are shown in Fig. 6a–d. In the case of pristine $BiVO_4$, as shown in Fig. 4a and b, Bi $4f_{7/2}$ and V $2p_{3/2}$ fitted well to main contributions from binding energies at ~159.08 eV and ~516.80 eV, respectively. The Bi $4f_{7/2}$ peak at 159.08 eV is characteristic of Bi^{3+} oxidation state [22], while the V $2p_{3/2}$ core-level spectrum represents a V^{5+} oxidation state. A similar fit was obtained for the $BiV_{0.95}Mo_{0.05}O_4$ sample. When the dopant concentration of Mo was at a value of x = 0.2, a distinctive shoulder could be observed for the Bi 4f spectra. The shoulder of the Bi $4f_{7/2}$ spectra for $BiV_{0.8}Mo_{0.2}O_4$ can be attributed to the presence of Bi^{5+} oxidation state. The peak at a binding energy of ~160.3 eV agrees with the values reported Bi^{+5} oxidation state [34] and [35]. The O 1s spectrum (Fig. 6d) has contribution from Sn-O in FTO. The main peak corresponding to $BiVO_4$ can be fitted at ~529.95 eV which is close to the surface lattice oxygen peak [22], [36] and [37]. The peak present at ~531 eV is ascribed to the nonstoichiometric oxygen (defective oxygen) [20] and [38]. This is due to the presence of Bi^{5+} state which can create a surface nonstoichiometry. In addition to lattice oxygen, presence of surface hydroxyl is shown from the fitted O1s peak at a binding energy of ~532.1 eV, that is typical for hydroxyl related species. Presence of Bi^{5+} state can induce the formation of surface hydroxyl groups on the surface of $BiVO_4$. The presence of surface hydroxyl groups can improve the surface wetting characteristics and reported in the literature [39] and [40]. This was further supported by the decrease in the contact angle (CA) values for $BiV_{0.8}Mo_{0.2}O_4$ (CA = 17.94° ± 1.29) compared to $BiVO_4$ (CA = 29.32° ± 2.25) and is shown as Fig. S7. The successful incorporation of Mo was observed from the Mo 3d peak observed for both $BiV_{0.95}Mo_{0.05}O_4$ and $BiV_{0.8}Mo_{0.2}O_4$ samples. The higher concentration of Mo in the $BiV_{0.8}Mo_{0.2}O_4$ can also be clearly seen from Fig. 6c, revealing increase in Mo incorporation. The binding energy of Mo $3d_{5/2}$ at 232.3 eV shows that Mo is present in a 6^+ oxidation state [37], [41] and [42].

The charge transport dynamics for water oxidation for the tetragonal $BiV_{0.8}Mo_{0.2}O_4$ and pristine Monoclinic $BiVO_4$ was further investigated by the electrochemical impedance measurements conducted under both dark and illuminated conditions at 1.23 V vs RHE as shown in Fig. 7a. The comparison was also made with the $BiV_{0.95}Mo_{0.05}O_4$ photoanode, which showed a reduction in the photocurrent compared to $BiV_{0.8}Mo_{0.2}O_4$ photoanode. Impedance spectra shows that the $BiV_{0.8}Mo_{0.2}O_4$ photoanode offered the least charge transfer resistance ($1.98 \times 10^4\ \Omega$ obtained by fitting the impedance spectra using R(RC) circuit) under illuminated conditions. $BiV_{0.95}Mo_{0.05}O_4$ photoanode showed higher resistance under illuminated conditions compared to pristine and $BiV_{0.8}Mo_{0.2}O_4$ samples, indicating the inefficiency in utilizing holes for efficient water oxidation compared to the $BiV_{0.8}Mo_{0.2}O_4$ photoanode. The open circuit potential measurements in dark and illumination conditions were further carried out to estimate the change in Fermi level of the pristine and doped samples under illumination [43]. Fig. 7b shows the plot of open circuit potential vs time for pristine $BiVO_4$, $BiV_{0.95}Mo_{0.05}O_4$ and $BiV_{0.8}Mo_{0.2}O_4$. Approximately 60 mV increase in the open circuit potential was observed for $BiV_{0.8}Mo_{0.2}O_4$ compared to pristine $BiVO_4$, and the difference in open circuit potential between dark and illuminated conditions were 0.12 V, 0.17 V and 0.28 V for pristine $BiVO_4$, $BiV_{0.95}Mo_{0.05}O_4$ and $BiV_{0.8}Mo_{0.2}O_4$ photoanodes respectively. This indicates the shift of Fermi level to a more cathodic region and hence enhanced charge separation under illuminated conditions. The observation thereby shows that, even though the $BiV_{0.8}Mo_{0.2}O_4$ was in the tetragonal crystal structure, the system was able to generate enhanced charge separation and thereby providing holes for water oxidation.

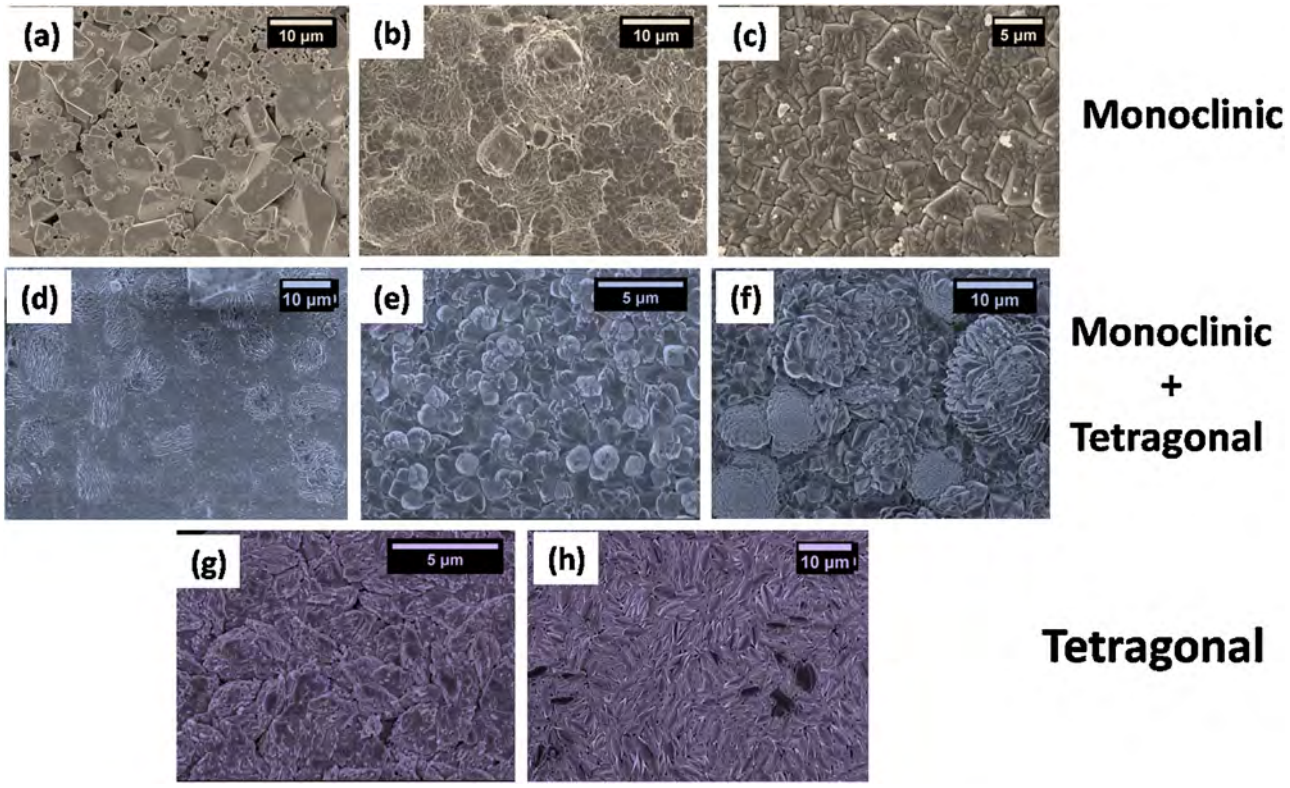

Fig. 3. FESEM micro graphs of (a) pristine, (b) $BiV_{0.99}Mo_{0.01}O_4$ (c) $BiV_{0.98}Mo_{0.02}O_4$ (d) $BiV_{0.97}Mo_{0.03}O_4$ (e) $BiV_{0.95}Mo_{0.05}O_4$ (f) $BiV_{0.92}Mo_{0.08}O_4$ (g) $BiV_{0.9}Mo_{0.1}O_4$ (h) $BiV_{0.8}Mo_{0.2}O_4$.

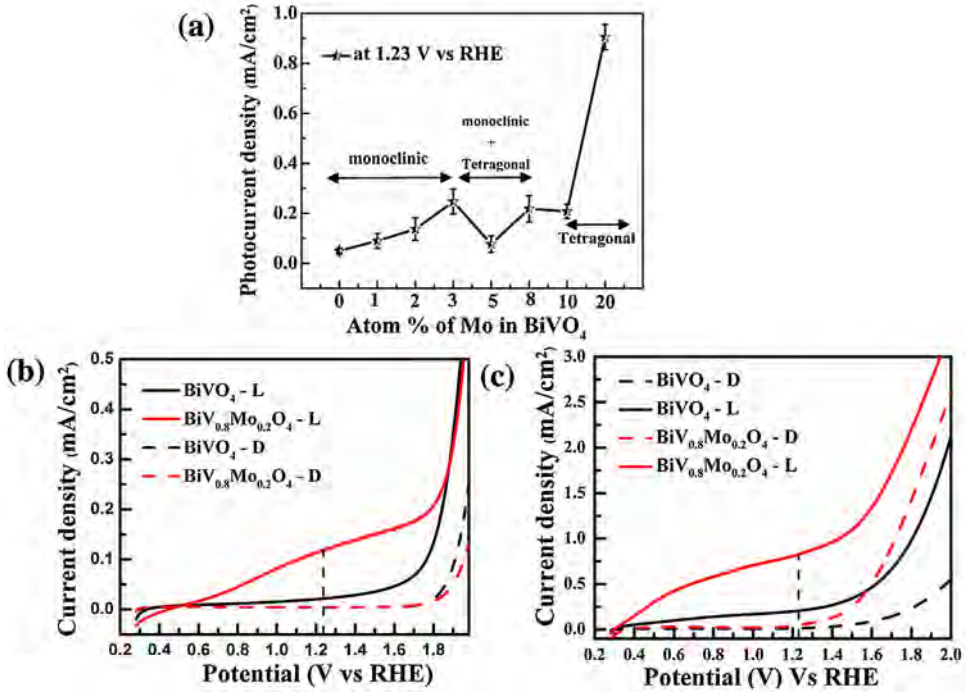

Fig. 4. (a) Variation of photocurrent at 1.23 V vs RHE in 0.5 M Na_2SO_4 + 0.5 M Na_2SO_3 (hole scavenger) with change in Mo doping concentration in $BiVO_4$ from x = 0 to 0.2 mol%(b) Linear sweep voltamograms for pristine $BiVO_4$ and $BiV_{0.80}Mo_{0.2}O_4$ under dark and illuminated conditions (a) in 0.5 M Na_2SO_4 electrolyte, (b) in 0.5 M Na_2SO_4 + 0.5 M Na_2SO_3 (hole scavenger).

Mott Schottky analysis was conducted for monoclinic $BiVO_4$ and tetragonal $BiV_{0.8}Mo_{0.2}O_4$ in sodium sulfate electrolytes under dark conditions as shown in Fig. S8. The slope of $BiV_{0.8}Mo_{0.2}O_4$ (8.1×10^{19} cm^{-3}) is slightly lower than the monoclinic $BiVO_4$ 5.6×10^{19} cm^{-3}) indicating a higher carrier concentration. Although a slight positive shift in the flat band potential (V_{fb}) was observed for the $BiV_{0.8}Mo_{0.2}O_4$, the effect of an increase in the carrier density was essentially cancelled out. The V_{fb} of the monoclinic $BiVO_4$ and tetragonal $BiV_{0.8}Mo_{0.2}O_4$ was calculated to be −0.602 and −0.535 V vs Ag/AgCl.

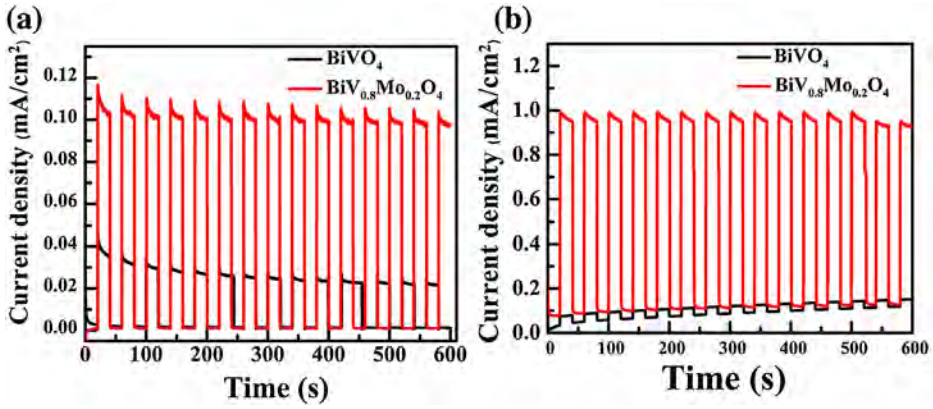

Fig. 5. Current vs time plot (a) in 0.5 M Na_2SO_4 at 1.23 V vs RHE (b) in 0.5 M Na_2SO_4 + 0.5 M Na_2SO_3 (hole scavenger), at 1.23 V vs RHE.

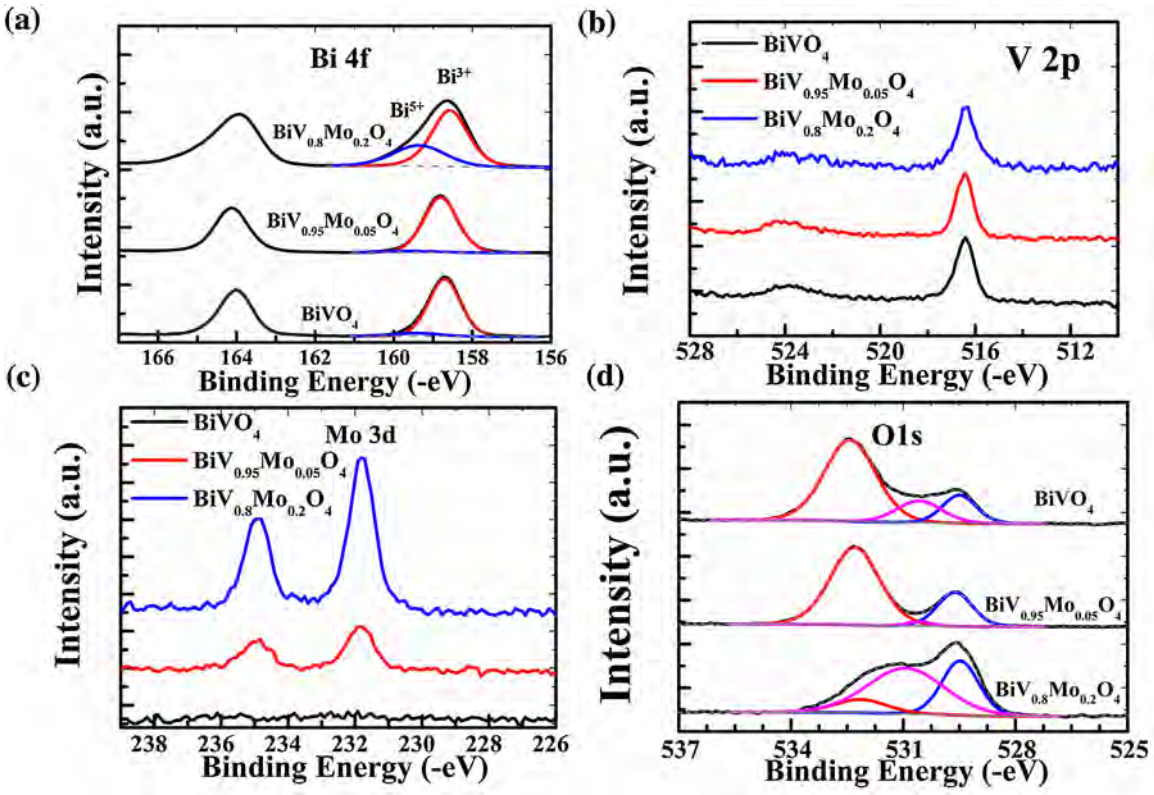

Fig. 6. High resolution X-ray photoelectron spectra of (a) Bi 4f, (b) V 2p, (c) Mo 3d and (d) O1s. The peak at ~531 eV correspond to the defective oxygen due to the presence of cationic vacancy.

Heterogeneous catalytic activity of scheelite tetragonal Mo doped $BiVO_4$ system increased as the atom fraction of Mo increased and obtained the highest activity in the range of x = 0.19 to 0.25 [44] and [45]. Tetragonal $Bi_{1-x/3}V_{1-x}Mo_xO_4$ system is known for better catalytic activity in oxidizing olefins due to increase in oxygen mobility and cation vacancies [44] and [46]. The solid solubility of Bi^{3+} vacancies can be tolerated up to 23% (x = 0.7) with the tetragonal crystal structure of $BiVO_4$ [26]. The cation vacancies and shared oxygen bonds associated with the presence of higher concentration Mo in the crystal lattice, favored electron hole separation. In the present study, based on the XPS, EIS and OCPV measurements, we propose the following mechanism. Presence of Bi^{5+} states in the $BiVO_4$ lattice can act as catalytic site for water oxidation reaction. The standard redox potential of Bi_V/Bi_{III} (E^o = +1.59 V at pH 0) [47] is more positive than O_2/H_2O (E^o = +1.23 V at pH 0) [30]. Hence, the existence of Bi^{5+} state in the present case helped to adjust the redox level positioning with respect to water oxidation potential, thereby increasing the rate of oxidation. The schematic of water oxidation mechanism in the presence of Bi_V/Bi_{III} redox system in tetragonal $BiV_{0.8}Mo_{0.2}O_4$ is shown in Fig. 7c. In addition, at higher dopant concentrations, the formation of rod-like morphology with reduction in size can provide more catalytically active sites for water oxidation and a better adhesion to the FTO glass. Even though the tetragonal $BiV_{0.8}Mo_{0.2}O_4$ displayed a higher band gap than the monoclinic polymorph, the presence of cationic vacancies, surface hydroxyl groups and a greater number of catalytic sites, improved charge separation, and hence gave a better PEC performance. The results suggested that introduction of cation vacancy due to higher concentration of Mo doping outweighed the adverse effect of formation of less catalytically active tetragonal phase formation by Mo doping.

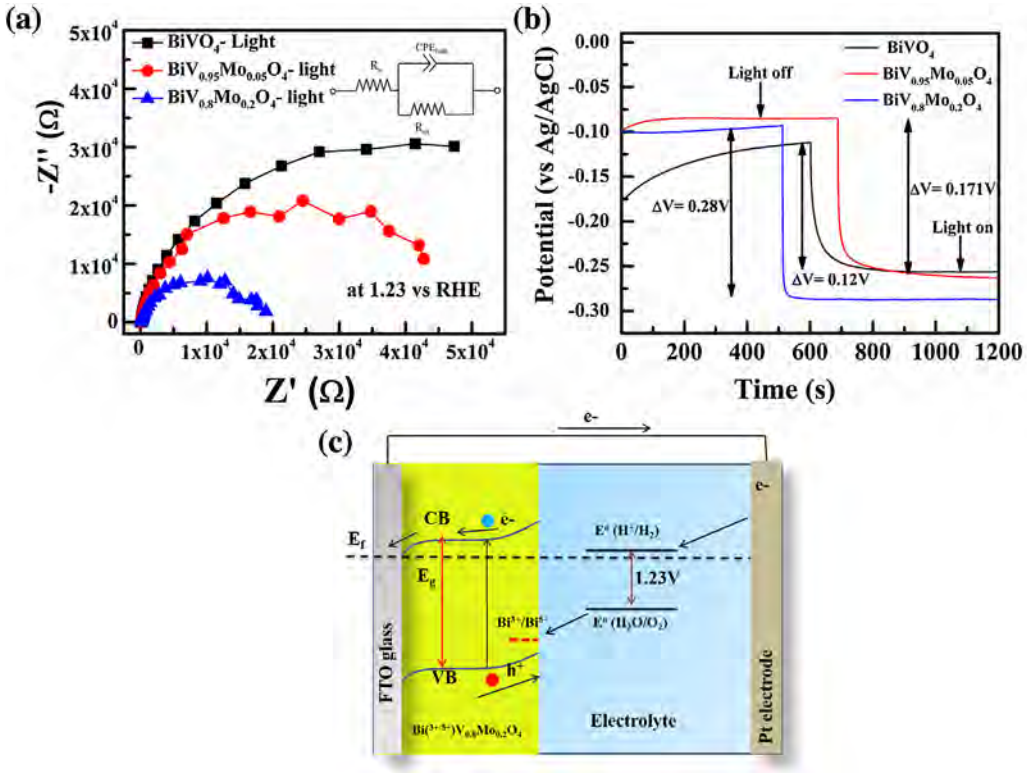

Fig. 7. (a) Electrochemical impedance spectra recorded at 1.23 V vs RHE in 0.5 M Na_2SO_4 electrolyte for pristine $BiVO_4$ and $BiV_{0.80}Mo_{0.2}O_4$, (b) The open circuit photovoltage vs Time plot for pristine $BiVO_4$, $BiV_{0.95}Mo_{0.05}O_4$ and $BiV_{0.80}Mo_{0.2}O_4$ in 0.5 M Na_2SO_4 electrolyte and (c) Schematic representation of photoelectrochemical water oxidation using tetragonal $BiV_{0.8}Mo_{0.2}O_4$ photoanode.

3. Conclusions

Mo:$BiVO_4$ was fabricated by hydrothermal synthesis. An enhancement in the photoelectrochemical performance was observed for the tetragonal $BiV_{0.8}Mo_{0.2}O_4$ photoanode, induced by higher amounts of Mo doping. This is attributed to the formation of cationic vacancies (Bi^{5+} states), and oxygen interstitials which was revealed from XPS analysis. Efficient charge transport and electron hole separation for water oxidation of $BiV_{0.8}Mo_{0.2}O_4$ photoanode was supported by electrochemical impedance investigations and open circuit photovoltage measurements. Our study thus throws light on to the role of cation vacancies in water oxidation reactions and hopefully provides an impetus for exploring the possibilities of increasing the photocatalytic and photoelectrochemical activities in other polymorphs of $BiVO_4$.

Appendix A. Supplementary data

Supplementary data associated with this article can be found, in the online version, at http://dx.doi.org/10.1016/j.apcata.2016.07.022.

References

[1] A. Fujishima, K. Honda, Nature 238 (1972) 37–38.
[2] K. Sivula, F. Le Formal, M. Grätzel, ChemSusChem 4 (2011) 432–449.
[3] P.S. Bassi Gurudayal, L.H. Wong, J. Barber, Phys. Chem. Chem.Phys. 16 (2014) 11834–11842.
[4] J.A. Seabold, K.-S. Choi, Chem. Mater. 23 (2011) 1105–1112.
[5] F.F. Abdi, R. van de Krol, J. Phys. Chem. C 116 (2012) 9398–9404.
[6] A. Kudo, K. Ueda, H. Kato, I. Mikami, Catal. Lett. 53 (1998) 229–230.
[7] J. Yu, A. Kudo, Adv. Funct. Mater. 16 (2006) 2163–2169.
[8] Z. Zhao, Z. Li, Z. Zou, Phys. Chem. Chem. Phys. 13 (2011) 4746–4753.
[9] F.F. Abdi, N. Firet, R. van de Krol, Chem. Cat. Chem. 5 (2013) 490–496.
[10] F.F. Abdi, R. van de Krol, J. Phys. Chem. C. 116 (2012) 9398–9404.
[11] D.K. Zhong, S. Choi, D.R. Gamelin, J. Am. Chem. Soc. 133 (2011) 18370–18377.
[12] S.K. Cho, H.S. Park, H.C. Lee, K.M. Nam, A.J. Bard, J. Phys. Chem. C 117 (2013) 23048–23056.
[13] W.J. Jo, J.-W. Jang, K. -j. Kong, H.J. Kang, J.Y. Kim, H. Jun, K.P.S. Parma, J.S. Lee, Angew. Chem. Int. 51 (2012) (2012) 3147–3151.
[14] C. Ding, J. Shi, D. Wang, Z. Wang, N. Wang, G. Liu, F. Xiong, C. Li, Phys. Chem. Chem. Phys. 15 (2013) 4589–4595.
[15] S. Ho-Kimura, S.J.A. Moniz, A.D. Handoko, J. Tang, J. Mater. Chem. A 2 (2014) 3948.
[16] S.J. Hong, S. Lee, J.S. Jang, J.S. Lee, Energy Environ. Sci. 4 (2011) 1781.
[17] Y. Hou, F. Zuo, A. Dagg, P. Feng, Nano Lett. 12 (2012) (2012) 6464–6473.
[18] S.J.A. Moniz, J. Zhu, J. Tang, Adv. Energy Mater. 4 (2014) 1301590.
[19] L. Shan, Y. Liu, J. Mol. Catal. A: Chem. 416 (2016) 1–9.
[20] L. Shan, H. Liu, G. Wang, J. Nanopart. Res. 17 (2015) 181.
[21] Y. Liang, T. Tsubota, L.P.A. Mooij, R. van de Krol, J. Phys. Chem. C 115 (2011) 17594–17598.
[22] S.K. Pilli, T.E. Furtak, L.D. Brown, T.G. Deutsch, J.A. Turner, A.M. Herring, Energy Environ. Sci. 4 (2011) 5028.
[23] S. Obregon, S.W. Lee, G. Colon, Dalton Trans. 43 (2014) 311–316.
[24] S. Obregón, G. Colón, Catal. Sci. Technol. 4 (2014) 2042.
[25] S. Usai, S. Obregón, A.I. Becerro, G. Colón, J. Phys. Chem. C 117 (2013) 24479–24484.
[26] D. Zhou, W.B. Li, L.X. Pang, J. Guo, Z.M. Qi, T. Shao, X. Yao, C.A. Randall, Dalton Trans. 43 (2014) 7290–7297.
[27] D. Zhou, L.-X. Pang, J. Guo, Z.-M. Qi, T. Shao, X. Yao, C.A. Randall, J. Mater. Chem. 22 (2012) 21412.
[28] R.D. Bayliss, S.S. Pramana, T. An, F. Wei, C.L. Kloc, A.J.P. White, S.J. Skinner, T.J. White, T. Baikie, J. Solid State Chem. 204 (2013) 291–297.
[29] R.L. Frost, D.A. Henry, M.L. Weier, W. Martens, J. Raman Spectrosc. 37 (2006) 722–732.
[30] A. Kudo, K. Omori, H. Kato, J. Am. Chem. Soc. 121 (1999) 11459–11467.
[31] R. Li, F. Zhang, D. Wang, J. Yang, M. Li, J. Zhu, X. Zhou, H. Han, C. Li, Nat. Commun. 4 (2013) 1432.
[32] G. Tan, L. Zhang, H. Ren, S. Wei, J. Huang, A. Xia, ACS App. Mater. Interfaces 5 (2013) 5186–5193.
[33] Y. Park, D. Kang, K.-S. Choi, Phys. Chem. Chem. Phys. 16 (2014) 1238–1246.
[34] H. Fan, G. Wang, L. Hu, Solid State Sci. 11 (2009) 2065–2070.
[35] Y. Li, J. Cheng, J. Song, J.A. Alonso, M.T. Fernández-Díaz, J.B. Goodenough, Chem. Mater. 24 (2012) 4114–4122.
[36] L. Zhang, D. Chen, X. Jiao, J. Phys. Chem. B 110 (2006) 2668–2673.
[37] D.S. Zingg, L.E. Makovsky, R.E. Tischer, F.R. Brown, D.M. Hercules, J. Phys. Chem. 84 (1980) 2898–2906.
[38] S. Sajjad, S.A.K. Legharia, J. Zhang, RSC Adv. 3 (2013) 1363–1367.

[39] G. Ketteler, S. Yamamoto, H. Bluhm, K. Andersson, D.E. Starr, D.F. Ogletree, H. Ogasawara, A. Nilsson, M. Salmeron, J. Phys. Chem. C 111 (2007) 8278–8282.
[40] R.P. Antony, T. Mathews, S. Dash, A.K. Tyagi, J. Phys. Chem. C 117 (2013) 6851–6860.
[41] J. Haber, T. Machej, L. Ungier, J. Ziółkowski, J.Solid State Chem. 25 (1978) 207–218.
[42] W. Yao, H. Iwai, J. Ye, Dalton Trans. (2008) 1426–1430.
[43] B.H. Meekins, P.V. Kamat, ACS Nano 3 (2009) 3437–3446.
[44] W. Ueda, K. Asakawa, C.-L. Chen, Y. Moro-oka, T. Ikawa, J. Catal. 101 (1986) 360–368.
[45] R. Kontic, G.R. Patzke, J. Solid State Chem. 189 (2012) 38–48.
[46] A.W. Sleight, W.J. Linn, Ann. N. Y. Acad. Sci. 272 (1976) 22–44.
[47] A.J. Bard, R. Parsons, J. Jordan, Standard Potentials in Aqueous Solution, 1st ed., M. Dekker, New York, 1985.